Supporting Information

Asymmetric Electronic Coupling in Fe–Cu Dual-Atom Sites Enables Accelerated Oxygen Electrocatalysis for High-Performance Zn–Air Batteries

Ze Lv [a], Yang Qiu [b], Jiawei Luo [a], Zheng Shu [c], Kaibing Xu [d], Linping Zhang [a], Hong Xu [a], Zhiping Mao [a,*]

a. *National Engineering Research Center for Dyeing and Finishing of Textiles, College of Chemistry and Chemical Engineering, Donghua University*
No.2999 North Renmin Road, Shanghai, 201620, China

b. *School of Chemical Engineering, Sichuan University, Chengdu, 610065, China*

c. *State Key Laboratory of Metal Matrix Composites, School of Materials Science and Engineering, Shanghai Jiao Tong University, Shanghai 200240, China*

DState Key Laboratory for Modification of Chemical Fibers and Polymer Materials, College of Materials Science and Engineering, Donghua University, Shanghai 201620, China

* Corresponding authors.

E-mail address: zhpmao@dhu.edu.cn (Zhiping Mao).

1 Experimental Details.

1.1 Chemicals. Potassium permanganate ($KMnO_4$, 98%, Alfa Aesar), manganese (II) sulfate monohydrate ($MnSO_4{\cdot}H_2O$, 99%, Alfa Aesar), Pyrrole (C_4H_5N, 99%, Innochem), aniline (C_6H_7N, 99%, Innochem), ammonium fluoride (NH_4F, 98.0%, Sigma-Aldrich Shanghai, Ferric chloride hexahydrate ($FeCl_3{\cdot}6H_2O$, Sigma-Aldrich Shanghai), Commercial (Pt/C, 20 wt%) catalyst was purchased from Shanghai Hesen Electric Co., Ltd. All the chemicals and reagents were used as received without further purification, and deionized (DI) water was used throughout the whole experiment.

1.2 Preparation of FeCu-NCNT catalyst.

Preparation of MnO_2 nano wires: Firstly, 3 mmol of $MnSO_4$, 2 mmol of $KMnO_4$, and 2 mmol of NH_4F were dissolved in 40 mL of deionized water under magnetic stirring to form a homogeneous solution. The solution was then transferred to a 50 mL Teflon-lined stainless-steel autoclave, which was subsequently placed in a convection oven at 150 °C for 12 hours. After the autoclave naturally

cooled to room temperature, the brown product was collected.

Preparation of PPy-co-PANI: 200 mg of MnO_2 nano wires were dispersed in 200 mL of 0.02 M H_2SO_4. Subsequently, 510 μL of C_4H_5N and 390 μL of C_6H_7N were added to the solution. After stirring for 6 hours, the product was collected by centrifugation using deionized water, followed by drying in an 80 °C oven for 24 hours.

Preparation of FeCu-NCNT: First, 100 mg of sodium dodecylbenzene sulfonate (SDBS) and 400 mg of PPy-co-PANI were dispersed in 20 mL of deionized water under continuous stirring for 6 hours. Subsequently, 86.54 mg of $FeCl_3 \cdot 6H_2O$, 53.55 mg $CuCl_2 \cdot 5H_2O$) was added to the above mixture, followed by stirring for an additional 24 hours. The resulting precipitate was collected via centrifugation, thoroughly washed with deionized water and ethanol to remove residual impurities, and dried under vacuum at 60 °C for 12 h. Finally, the obtained product was thermally annealed at 900 °C for 2 hours under a high-purity argon flow (heating rate: 5°C min^{-1}) to yield the FeCu-NCNT. The synthesis of Fe-/Cu-NCNT are similar to the FeCu-NCNT except without adding Cu/Fe.

1.3 Characterization techniques.

The structural characteristics of the prepared materials were examined using multiple techniques: scanning electron microscopy (SEM, S-4800) operated at 5 kV, transmission electron microscopy (TEM, JEM-2100/JEM-2100F) at 200 kV/800 kV, and aberration-corrected HADDF-STEM (JEM-ARM300) at 300 kV. X-ray diffraction (XRD) analyses were conducted using a Bruker D8 ADVANCE instrument. X-ray photoelectron spectroscopy (XPS) measurements were acquired using an Escalab 250Xi, with all recorded binding energy data calibrated using C 1s (284.8 eV) as the reference to analyze the chemical composition. The DXR2xi Raman spectrometer was employed for Raman spectroscopy. The specific surface area was determined by analyzing the N_2 adsorption/desorption isotherms (Autosorb-iQ) according to the Brunauer-Emmett-Teller (BET) method. The iron content was assessed using an inductively coupled plasma optical emission spectrometer (ICP-OES, Agilent 5110). The Fe and Co K-edge X-ray absorption spectra (XAS) were recorded at the BL14W1 beamline of the Shanghai Synchrotron Radiation Facility.

1.4 Electrochemical measurements.

All the electrochemical measurements were conducted in 0.1 mol L^{-1} KOH electrolyte using a three-electrode system operated on an electrochemical workstation (CHI760E). The working

electrode were the rotating disk electrode (RDE) with a glass carbon disk of 5 nm diameter. The graphite rod electrode and Hg/HgO electrode (1 mol L^{-1} KOH solution) were used as a counter electrode and reference electrode. The recorded potential values vs. Hg/HgO were converted to a reversible hydrogen electrode (RHE) scale according to the Nernst equation ($E_{RHE} = E_{Hg/HgO} + 0.059 \times pH + 0.098$). For the working electrode preparation, 5mg catalyst sample were dispersed in 450 μL ethanol 50 μL 5 wt% Nafion by sonication for 1 h. The prepared catalyst ink was coated on the rotating disk electrode with a mass catalyst load of 0.5 mg cm^{-2} followed by air drying.

The cyclic voltammetry (CV) was performed in N_2 and O_2-saturated 0.1 M KOH solution with a sweep rate of 50 mV s^{-1}. The linear sweep voltammetry (LSV) curves were recorded in O_2 saturated electrolyte at 5 mV s^{-1} in rotating speed of 1600 rpm. The polarization curve of LSV at a scanning rate of 10 mV s^{-1} was recorded in 0.1 M KOH solution with a rotating speed of 400 rpm ~ 2025 rpm. The electrochemical active surface area (ESCA) of the catalyst was evaluated by measuring the double layer capacitance at different scanning rates (2 to 10 mV s^{-1}) in the non-Faraday potential range using CV curves. The solution resistance (Rs) was obtained from electrochemical impedance spectroscopy (EIS), and 95% IR compensation was applied to all OER polarization curves unless otherwise stated.

Stability was characterized both by accelerated aging test and CV. The former compared the LSV curves before and after cycling in the potential range of 0.6~1.0 V vs. RHE for 5000 cycles. For the current-time chronoamperometric test, O_2 was bubbled into 0.1 M KOH electrolyte for 30 min prior to the experiment and a flow of O_2 was maintained over the electrolyte during the test to ensure O_2 saturation. The test process was constant at 0.9 V vs. RHE. (Supporting Information)

The kinetic parameters of the ORR can be analyzed through the Koutecky - Levich (K-L) plots by

$$\frac{1}{j} = \frac{1}{j_k} + \frac{1}{j_l} = \frac{1}{B\omega^{1/2}} + \frac{1}{j_k} \qquad (1)$$

$$B = 0.2nFC_o D_o^{2/3} \qquad (2)$$

The measured current density is expressed as j, the kinetic current density is j_k, the diffusion limited current density is j_l, the electrode speed (rpm) is ω, the electron transfer number of O_2 is n,

the Faraday constant (96485 C mol^{-1}) is F, and the volume concentration of O_2 (7.8×10^{-7} mol cm^{-3}) is C_{O2}. The kinetic viscosity of the electrolyte (0.01 cm^2 S^{-1}) is υ and the diffusion factor of O_2 at 0.1 M KOH is 1.8×10^{-5} cm^2 S^{-1}.

Stability was characterized both by accelerated aging test and CV. The former compared the LSV curves before and after cycling in the potential range of 0.6~1.0 V vs. RHE for 5000 cycles. For the current-time chronoamperometric test, O_2 was bubbled into 0.1 M KOH electrolyte for 30 min prior to the experiment and a flow of O_2 was maintained over the electrolyte during the test to ensure O_2 saturation. The test process was constant at 0.9 V vs. RHE.

1.5 Zn-air battery assembly and measurements.

Synthesis of polyacrylamide-dimethyl sulfoxide (PAM-DMSO) hydrogel electrolyte: the hydrogel electrolyte was prepared as follows: 4 g of acrylamide (AM), 4 mg of N, N′-methylenebisacrylamide (MBAA, Crosslinking agent), and 10 mg of potassium persulfate ($K_2S_2O_8$, Initiator) were dissolved in 7 mL H_2O and 3 mL dimethyl sulfoxide under magnetic stirring at 500 r min^{-1}. The resultant solution was poured into a transparent rectangular mold, which was then sealed and placed in a 60°C oven for 4 hours. The as-prepared PAM-DMSO hydrogel (thickness of 0.3 cm) was immersed in the 6 M KOH + 0.2 M $Zn(Ac)_2{\cdot}6H_2O$ electrolyte for 72 h before use.

The electrochemical testing of ZAB was conducted in the electrochemical workstation (CHI660E) of the dual electrode system and in the ambient air of the Neware battery measurement system. The LSV curve records the discharge and charging curves of a half ZAB with an air cathode at room temperature. The constant current discharge, rate performance, and charge discharge cycle (10 minutes discharging followed by a 10 minutes charging.) of the battery were recorded on the Neware battery tester.

2. Computational Details

The DFT calculations were performed using the projector-augmented wave (PAW) pseudo-potentials in the Vienna *ab initio* Simulation Package (version 5.4.4) code.[1, 2] The Perdew–Burke–Ernzerhof (PBE) form of the generalized gradient approximation (GGA) was used to depict the exchange-correlation functional with a plane-wave cutoff energy of 450 eV.[3, 4] The structures in ORR process were fully optimized with single Γ point by the conjugate-gradient (CG) algorithm until the total energy and Hellmann-Feynman force are less than 1×10^{-5} eV and 0.05 eV $Å^{-1}$, respectively. For static calculations, a 2 × 2 × 1 *k*-point mesh and a denser 3 × 3 × 1 *k*-point mesh

within Monkhorst-Pack scheme were used to obtain the system's total energy and calculate the projected density of states (pDOS), respectively. To avoid the periodic interaction, a ~15 Å vacuum layer was adopted in the *z*-axis, and the van der Waals dispersion correction was considered via the DFT-D3 method.[5] All geometric structures were visualized using the VESTA package.

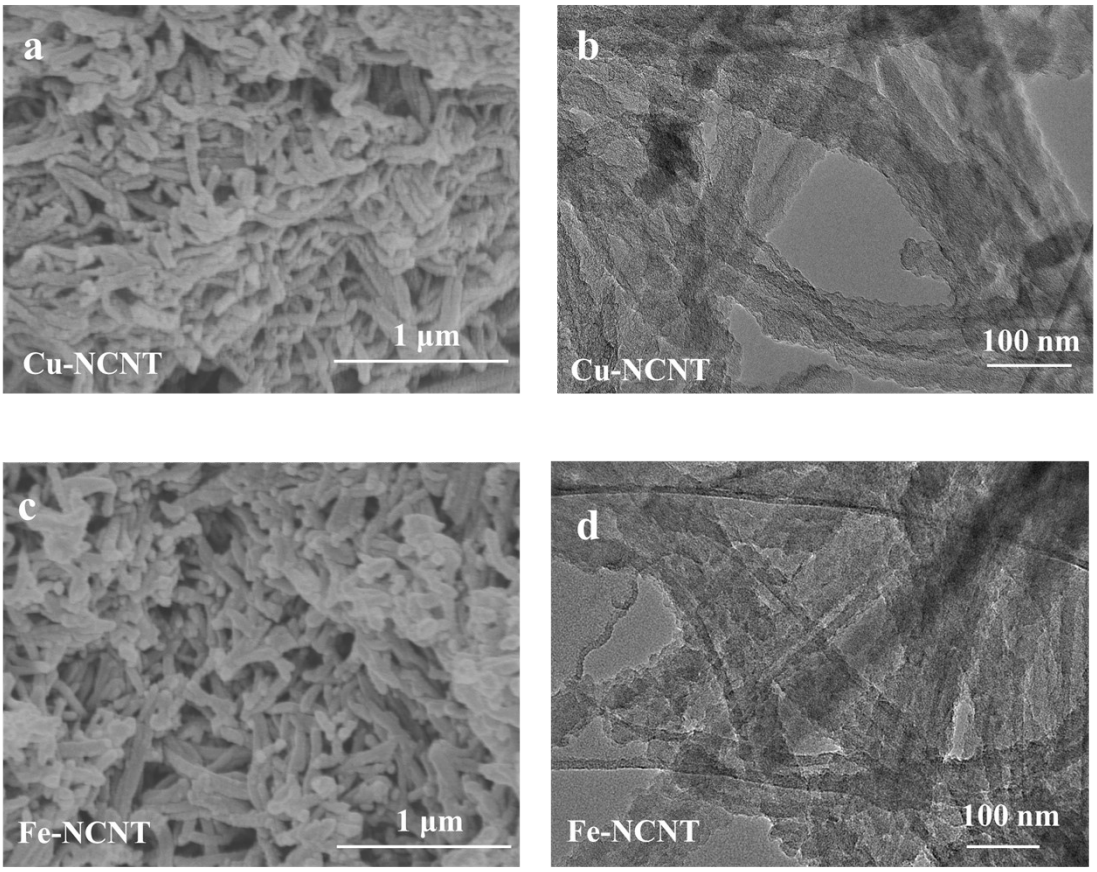

Figure S1. SEM and TEM of Fe-N_4 (a, b), Cu-N_4 (c, d), and NCNT (e, f).

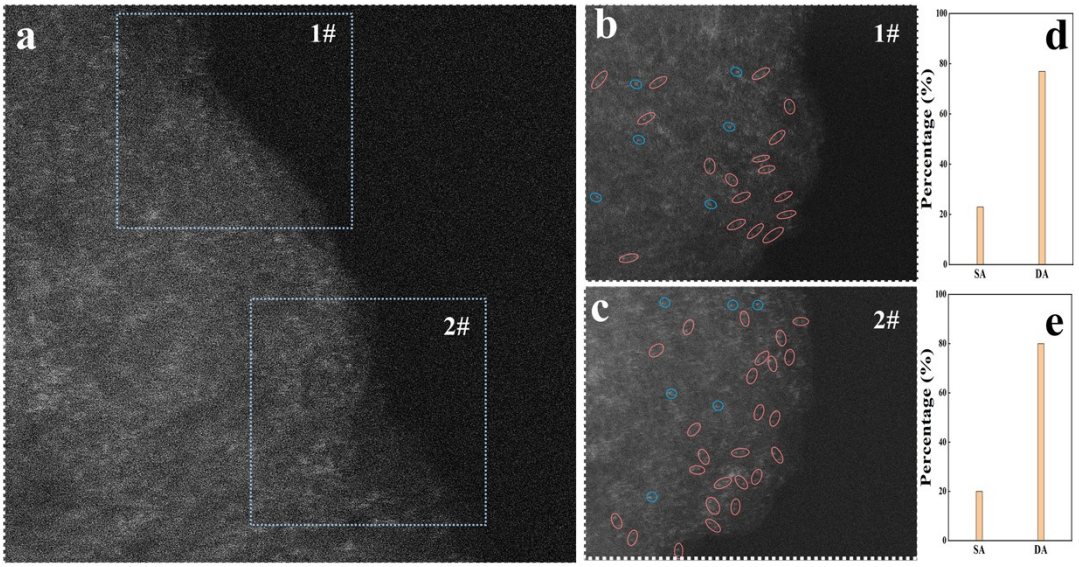

Figure S2. (a) HADDF-STEM image of FeCu-NCNT; (b, c) AC-HAADF-STEM images of FeCu-NCNT obtained in (a); (d, e) Statistical study of the single-atom (SA, blue circles) and dual-atom (DA, pink rectangles) in b and c.

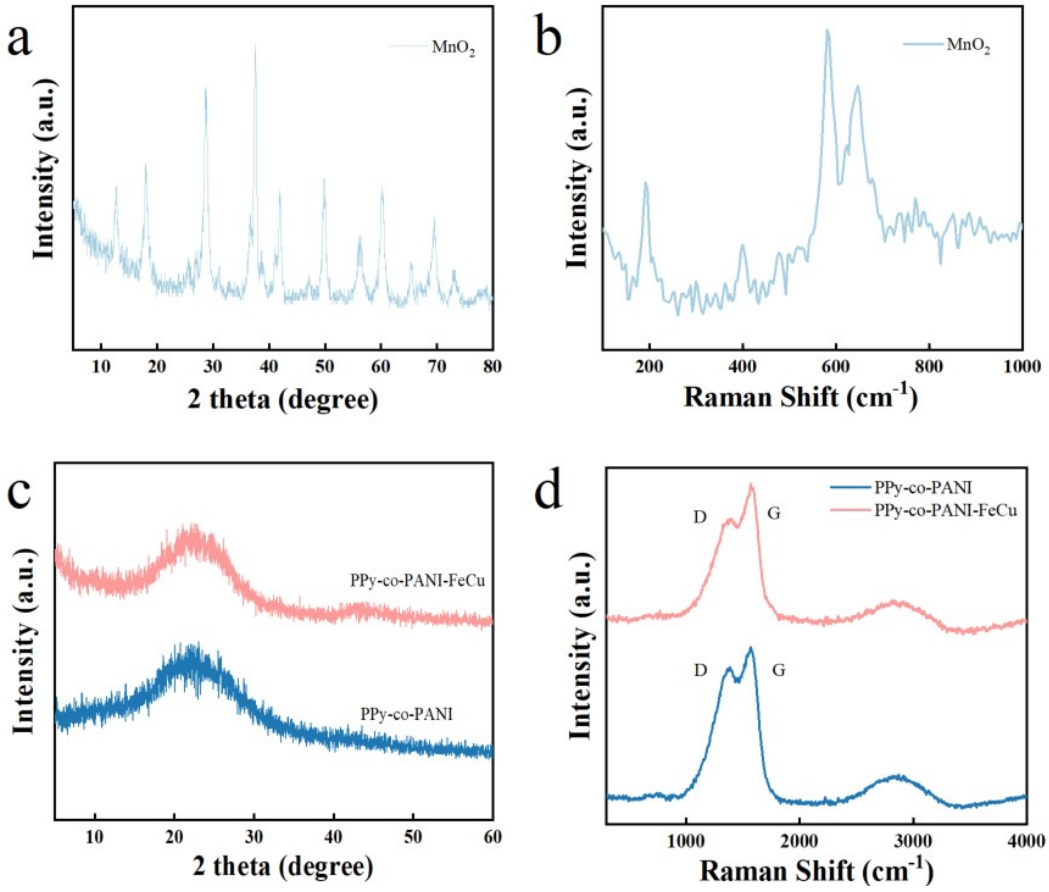

Figure S3. XRD patterns of MnO_2, PPy-co-PANI, and PPy-co-PANI-Fe, (c)Raman patterns of

MnO_2, PPy-co-PANI, and PPy-co-PANI-Fe.

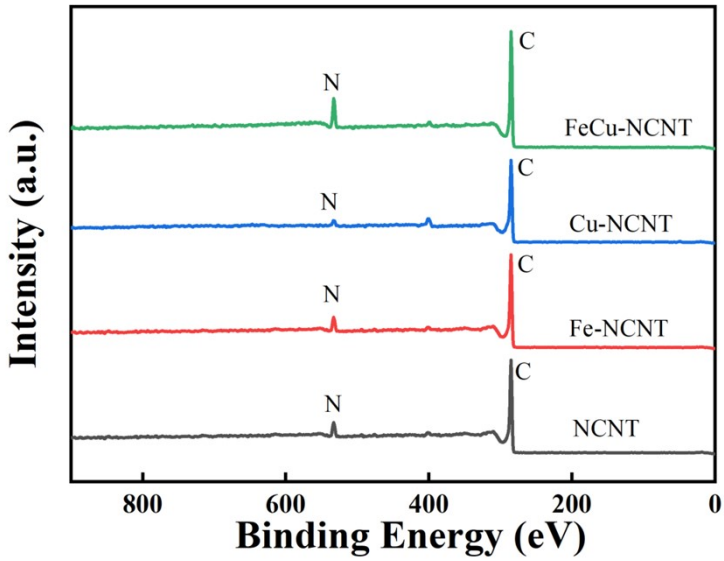

Figure S4. XPS spectra of FePc-Fe-NCNT, FePc-NCNT, Fe-N_4-NCNT, and NCNT.

In our synthesis, MnO_2 nanowires were used as both an oxidant and a reactive hard template for constructing the conjugated polymer precursor (PPy-co-PANI) through the copolymerization of pyrrole and aniline (Ref: *Small* 2018, *14*, 1703950; *Nat. Commun.* 2015, *6*, 7221). Notably, the redox potential of MnO_2 (Mn^{4+}/Mn^{2+}, 1.224 V vs SHE) is significantly higher than the redox polymerization potentials of pyrrole and aniline (<0.7 V vs SHE) (Ref: *Acc. Chem. Res.* 2008, *41*, 699−707). Therefore, MnO_2 effectively initiated the oxidative polymerization of the monomers at the solid–liquid interface. Simultaneously, MnO_2 served as a morphological template, enabling the growth of PPy-co-PANI on its surface. During the redox polymerization process, MnO_2 was consumed via the reaction $MnO_2 + 4H^+ + 2e^- \rightarrow Mn^{2+} + 2H_2O$ (Ref: *Adv. Mater.* 2007, *19*, 461−464), ultimately resulting in the formation of hollow-structured PPy-co-PANI.

To verify the complete removal of Mn-containing species, we conducted XRD and Raman spectroscopy analyses of the intermediates PPy-co-PANI and PPy-co-PANI-Fe (Figure S2). Neither the XRD patterns nor the Raman spectra exhibit any detectable MnO_2-related peaks, indicating that MnO_2 was fully consumed during synthesis. Furthermore, as shown in Figure S3, XPS survey spectra of all four final catalysts display no Mn-related characteristic peaks, further confirming the absence of residual Mn in the materials. Taken together, these results demonstrate that MnO_2 served only as a temporary oxidizing template and was fully removed during the synthesis. Therefore, the observed ORR activity originates exclusively from the FeCu-NCNT active centers, without

interference from residual Mn species.

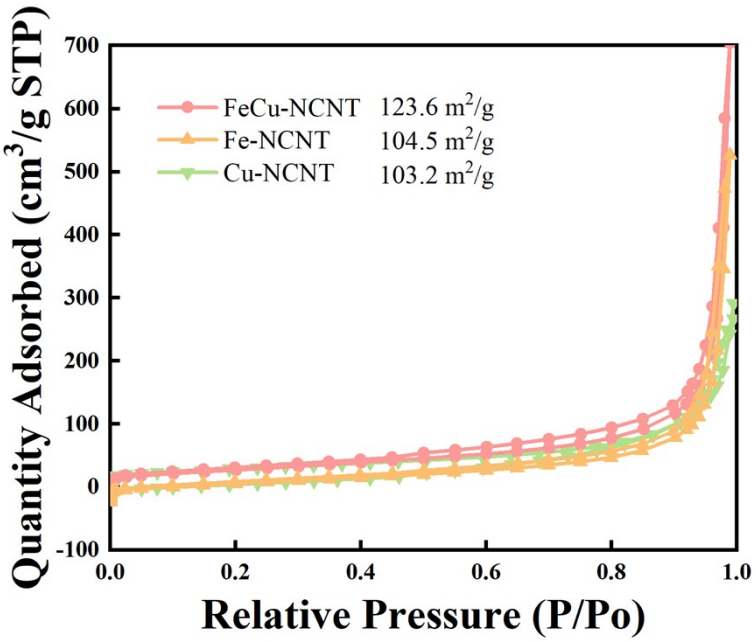

Figure S5. Nitrogen adsorption and desorption curves of different prepared catalysts.

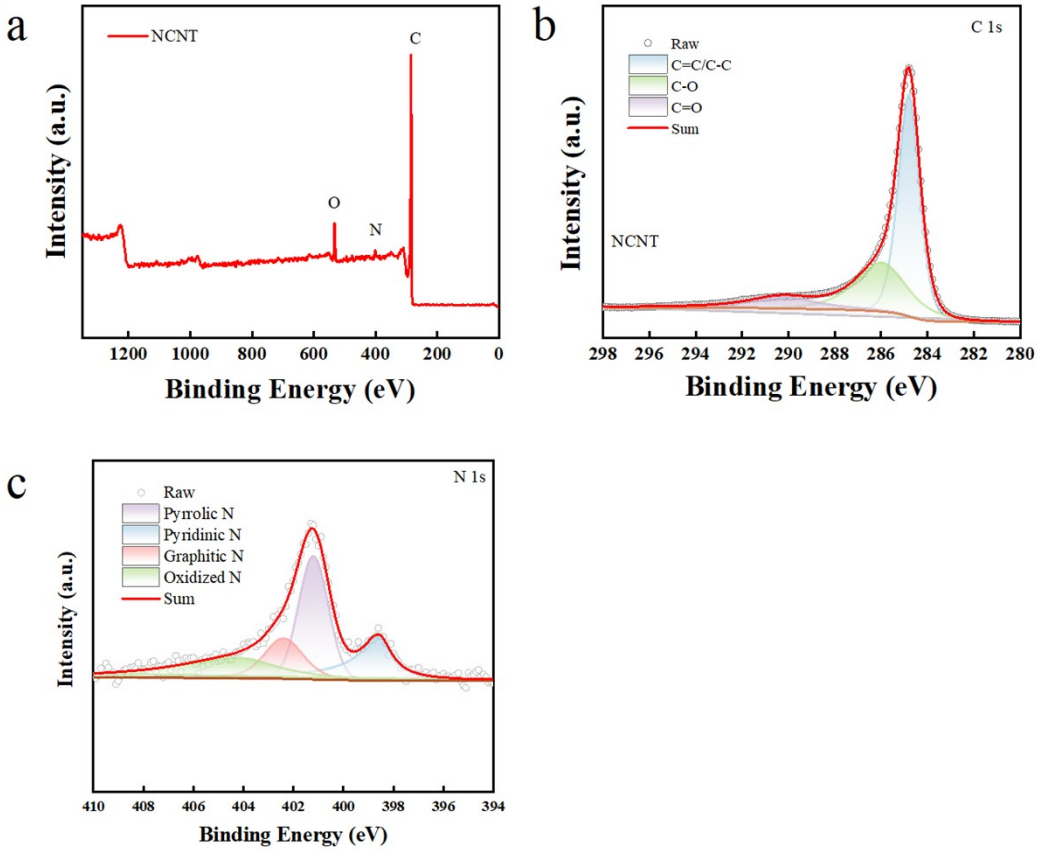

Figure S6. The XPS spectra for all (a), C 1s (b), N 1s (c) of NCNT.

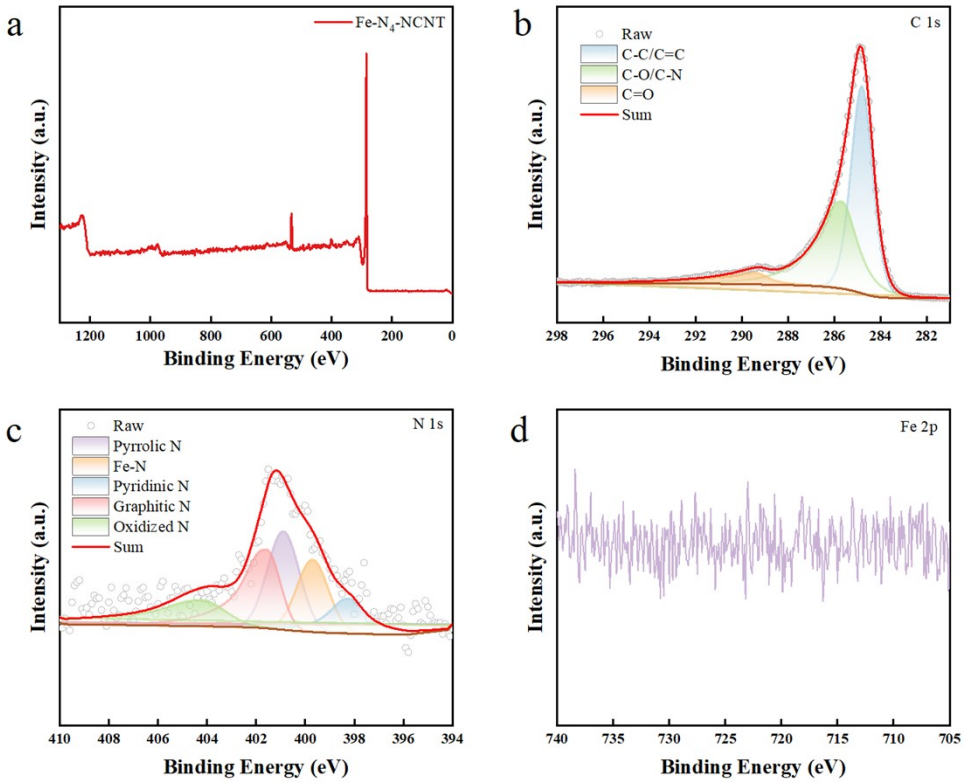

Figure S7. The XPS spectra for all (a), C 1s (b), N 1s (c), and Fe (d) of Fe-NCNT.

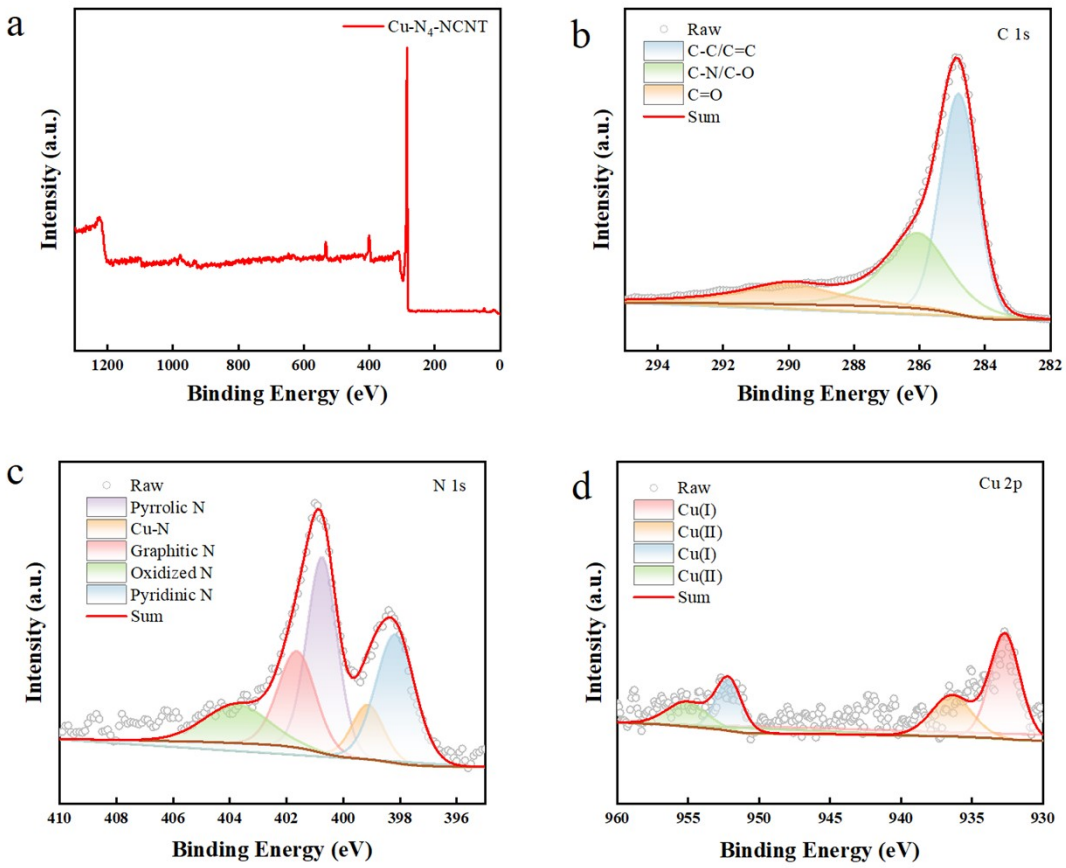

Figure S8. The XPS spectra for all (a), C 1s (b), N 1s (c), and Cu (d) of Cu-NCNT.

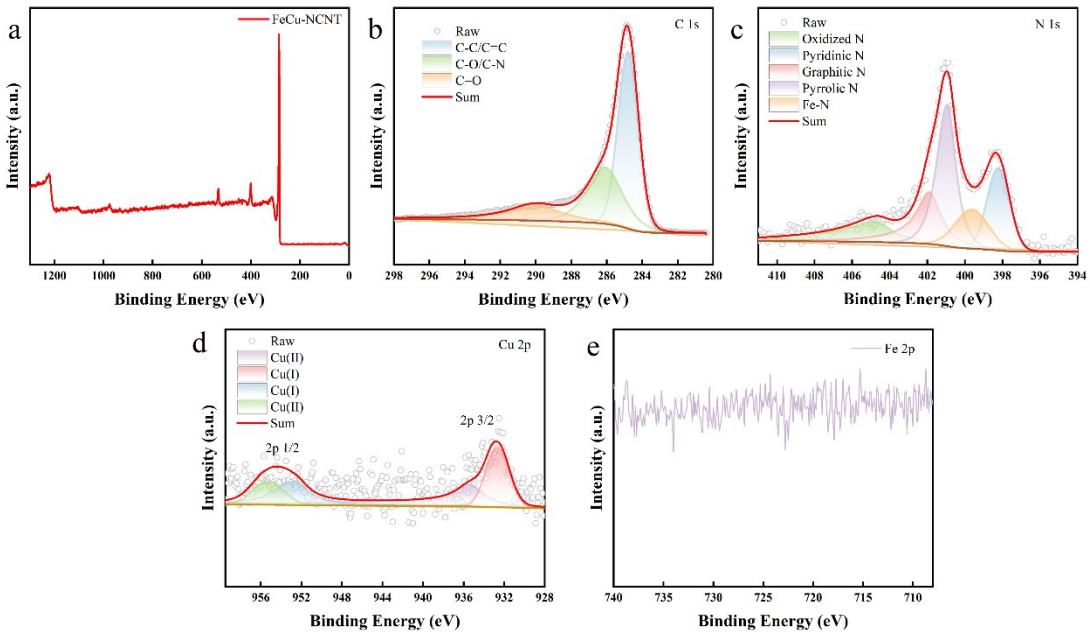

Figure S9. The XPS spectra for all (a), C 1s (b), N 1s (c), Cu (d) and Fe (e) of FeCu-NCNT.

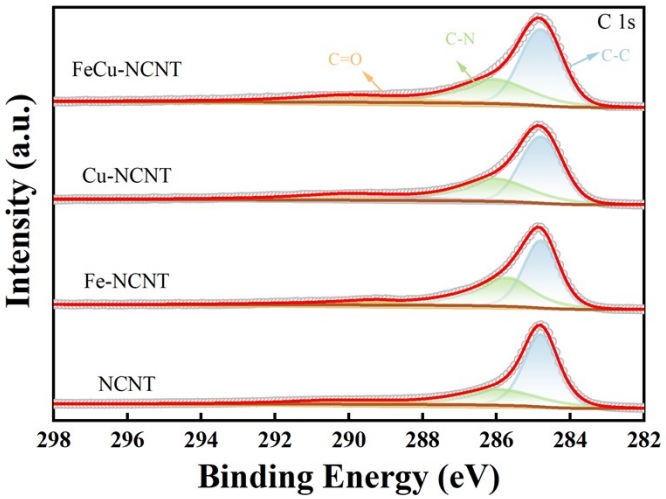

Figure S10. High-resolution C 1 spectra of different prepared catalyst.

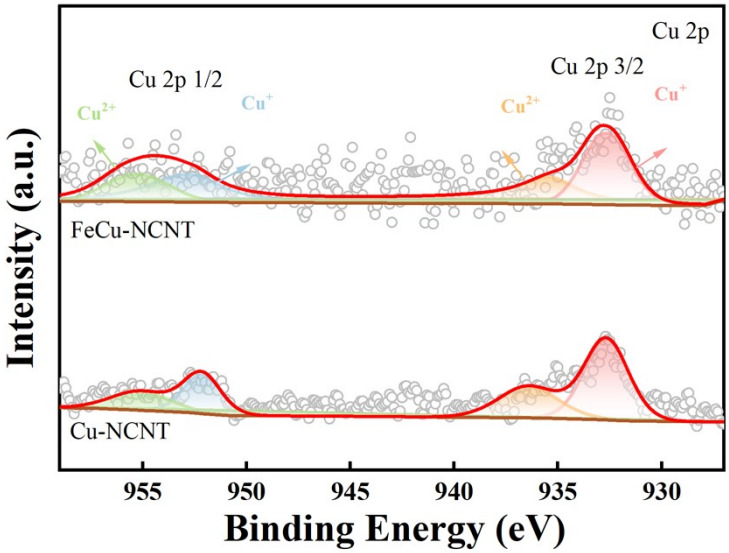

Figure S11. High-resolution Cu 2p spectra of different prepared catalyst.

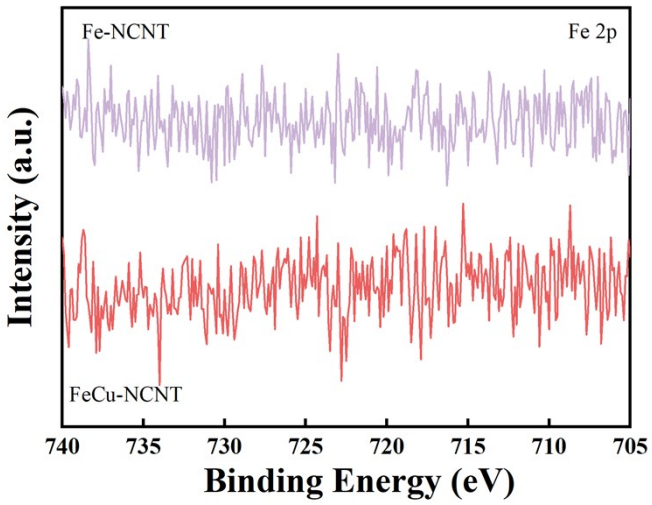

Figure S12. High-resolution Fe 2p spectra of different prepared catalyst

The weak Fe XPS signals can be attributed to the low metal loadings and atomic dispersion of the active sites, which are close to the detection limit of XPS.

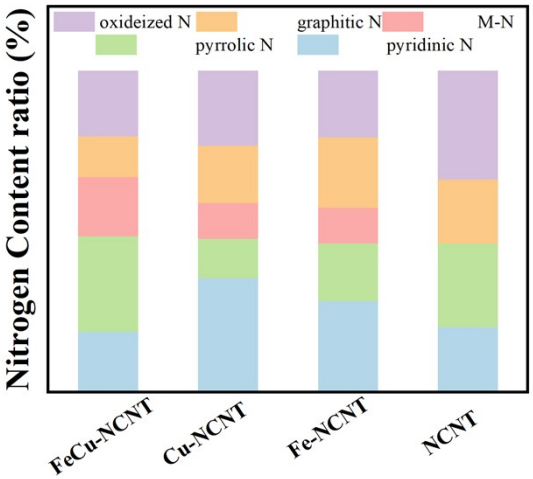

Figure S13. The N content distribution of FeCu-NCNT, Fe-NCNT, Cu-NCNT and NCNT.

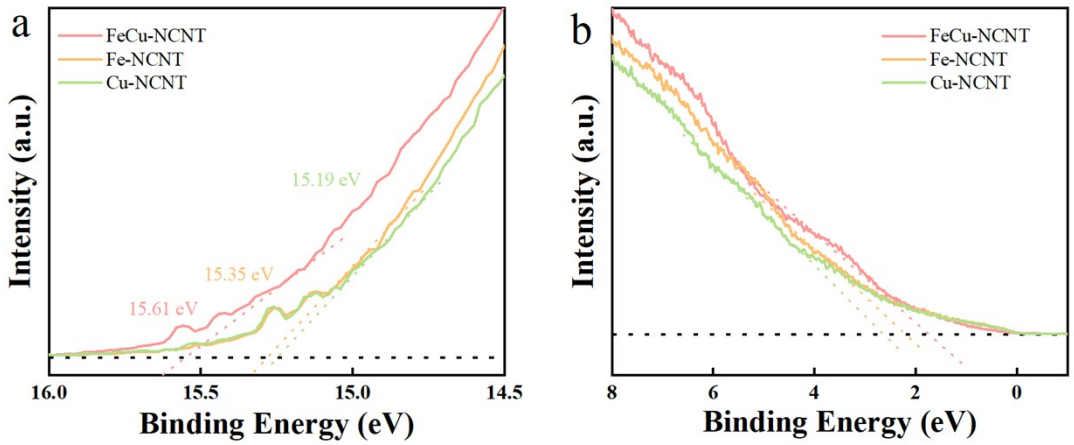

Figure S14. (a) Valence-band spectrum of FeCu-NCNT, Fe-NCNT and Cu-NCNT; (bb) the work functions of FeCu-NCNT, Fe-NCNT and Cu-NCNT

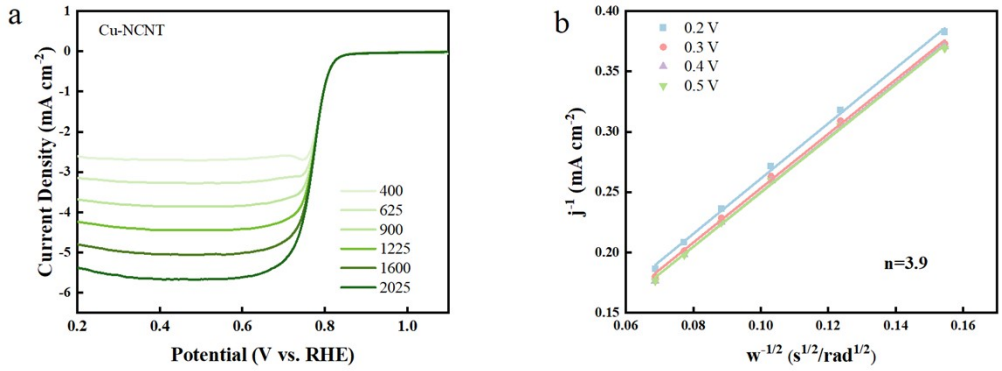

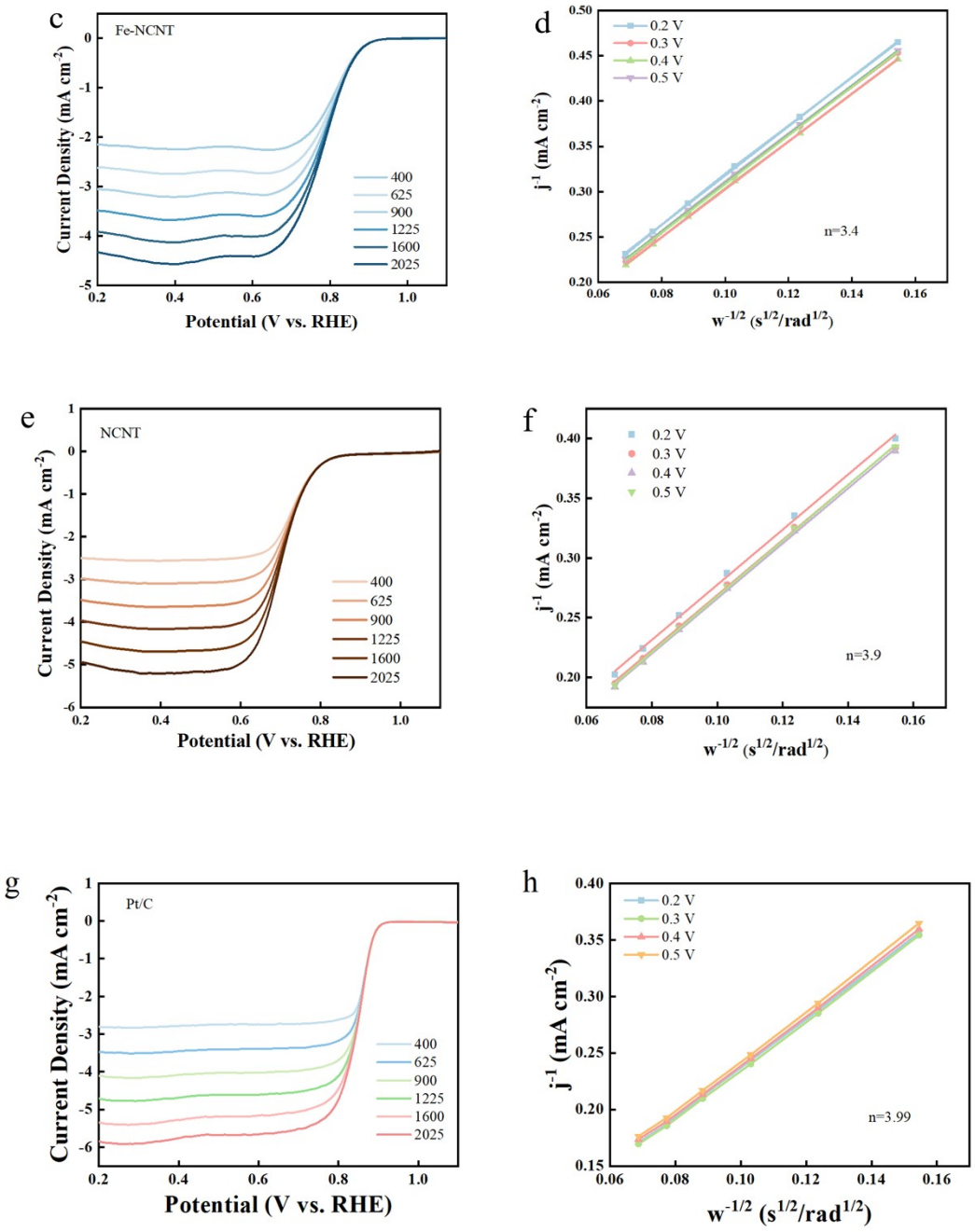

Figure S15. The ORR polarization curves of Fe-NCNT (a, b); Cu-NCNT (c, d); NCNT (e, f); Pt/C (g, h) at different rotating rates with K-L plots and electron transfer number.

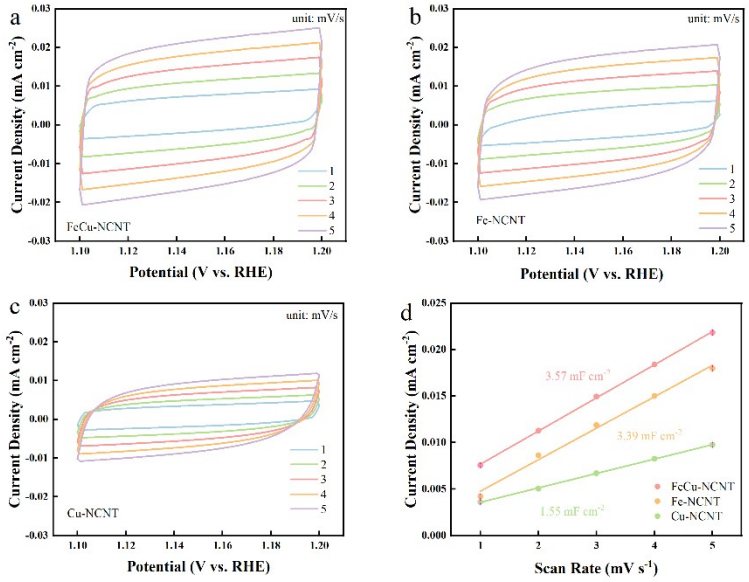

Figure S16. ORR CV curves of different catalysts in O_2-saturated 0.1 M KOH at different scan rates (2-10 mV s^{-1}) in 1.10-1.20 V vs RHE for ORR (a-d), and corresponding electrochemical double-layer capacitance (C_{dl}) (e).

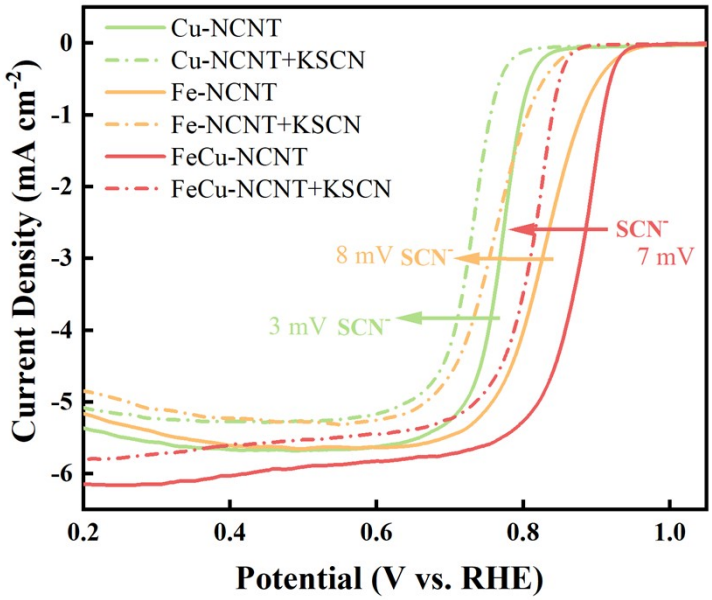

Figure S17. The complete LSV curves for the ORR activity loss after adding 10 mM KSCN into electrolyte.

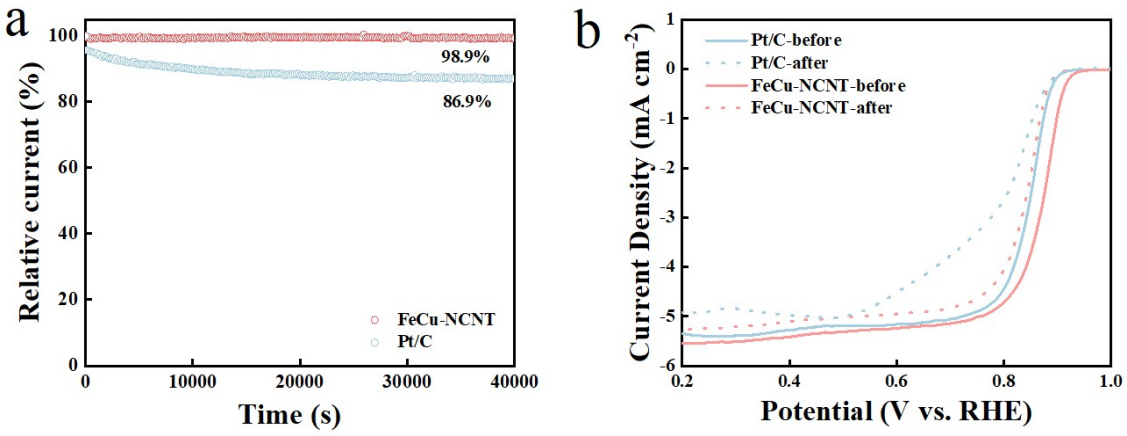

Figure S18. (a) Chronoamperometric curves of FeCu-NCNT and 20% Pt/C; (b) ORR polarization curves after 5000 cycles of FeCu-NCNT and 20% Pt/C.

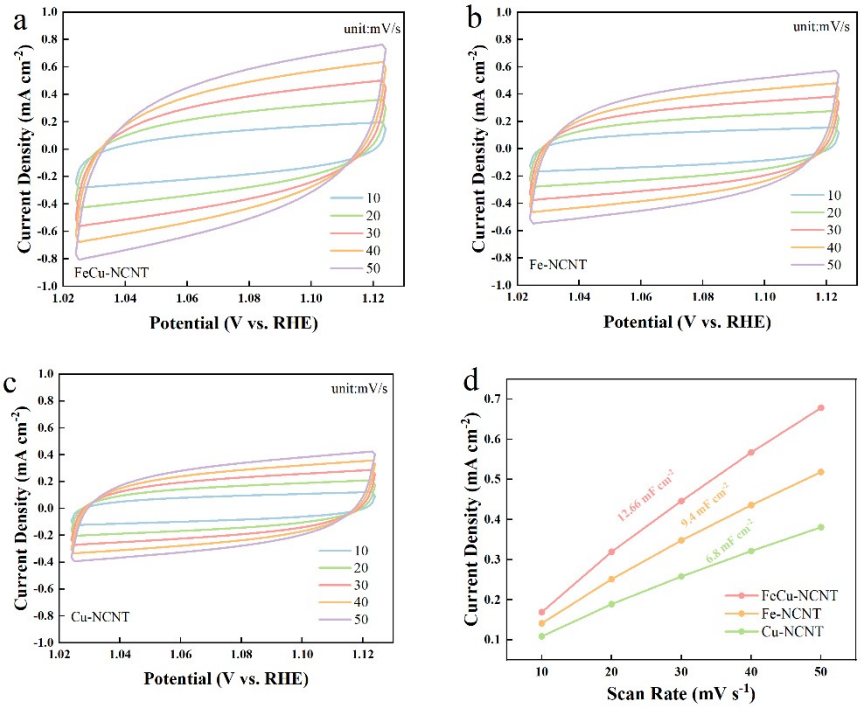

Figure S19. OER CV curves of different catalysts in O_2-saturated 0.1 M KOH at different scan rates (10-50 mV s^{-1}) in 1.08-1.13V vs RHE for OER (a-d), and corresponding electrochemical double-layer capacitance (C_{dl}) (e).

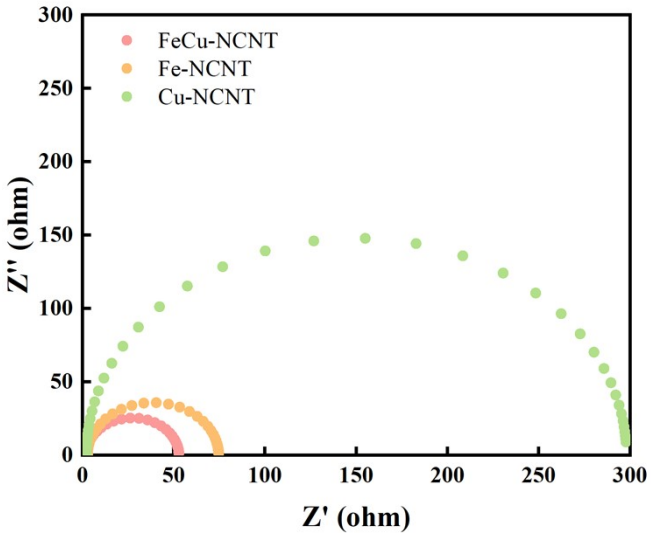

Figure S20. EIS of FeCu-NCNT, Fe-NCNT, and Cu-NCNT.

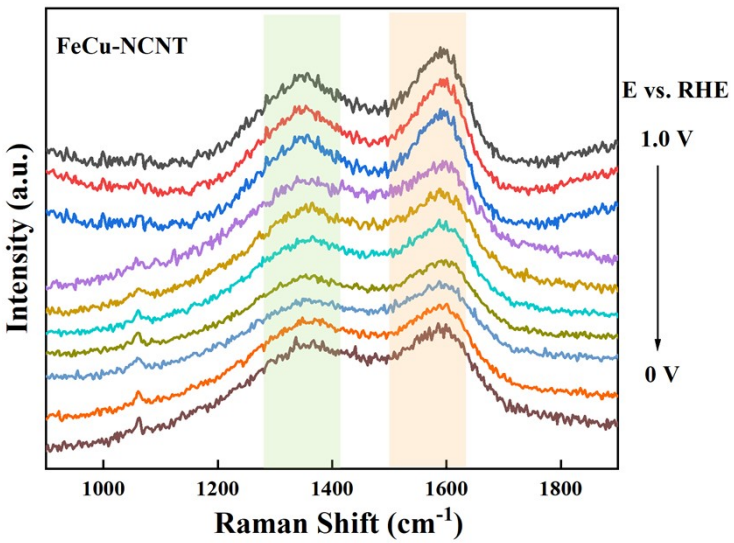

Figure S21. In situ Raman spectra of FeCu-NCNT catalysts.

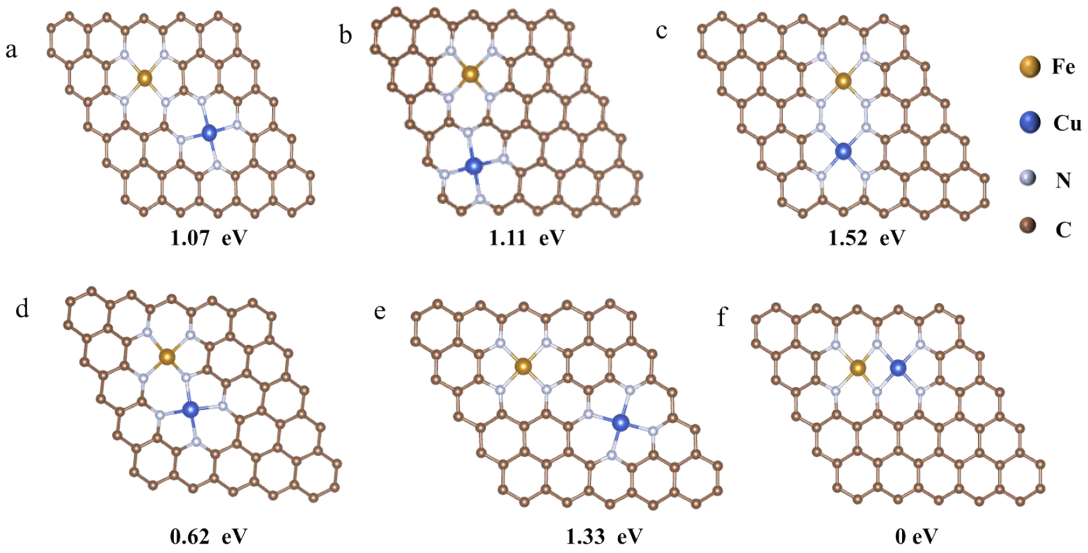

Figure S22. Computed structural models of Fe-N_4/Cu-N_4. The most stable model is used as energy reference as displayed in Figure S22d.

It was shown that the models in Figure S22(a–e) are less thermodynamically stable than the model in Figure S22d. This result indicates that the FeCu–N_6 dual-site structure represents the most stable local coordination environment [6].

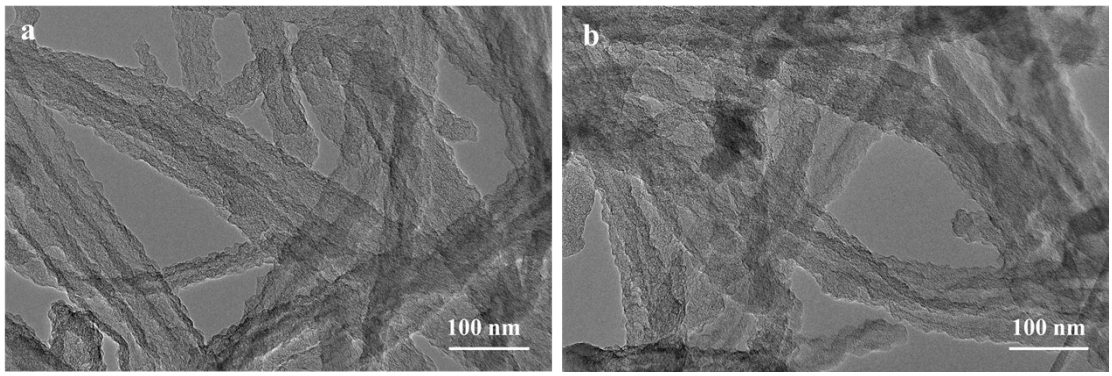

Figure S23. TEM of FeCu-NCNT after charge-discharge test.

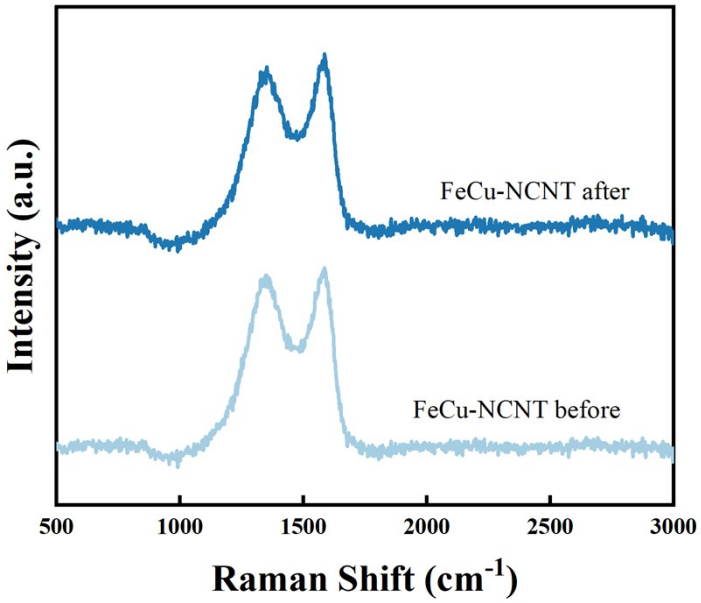

Figure S24. Raman spectra of FeCu-NCNT catalyst.

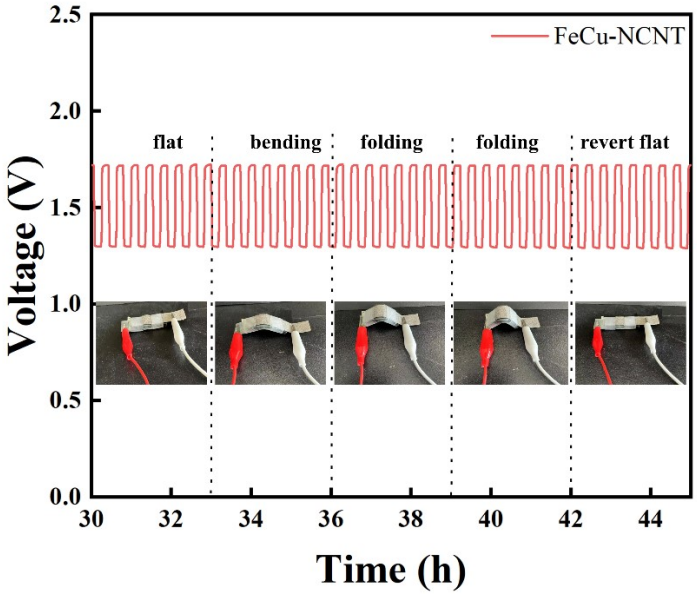

Figure S25. Galvanostatic charge/discharge curve of the QSS-ZABs assembled FeCu-NCNT under various mechanical deforms.

Table S1. Cu-EXAFS data fitting results of FeCu-NCNT.

Sample	Scattering pair	CN	R (Å)	σ^2 (Å^2)	ΔE_0 (eV)	R-factor
FeCu-NCNT	Cu-N1	1.8	1.901+0.06	0.003	8.27	0.001
	Cu-N2	2.1	1.936+0.15	0.0015		
	Cu-Fe	0.8	2.508+0.39	0.002		
Cu-NCNT	Cu-N	3.78	1.92+0.022	0.007	5.8	0.0023

CN represents coordination number, R represents interatomic distance, σ^2 indicates the Debye-Waller factor value, ΔE_0 represents edge-energy shift, and R-factor represents goodness of the fit. Error bounds (accuracies) that characterize the structural parameters obtained by EXAFS spectroscopy were estimated as CN ± 20%; R ± 1%; σ^2 ± 20%; ΔE_0 ± 20%. S_0^2 was fixed to 1.0, which is according to the experimental EXAFS fit of Fe foil by fixing CN as the known crystallographic value. Fitting range: 2.0 ≤ k (/Å) ≤ 12.5 and 1≤ R (Å) ≤ 4; A reasonable range of EXAFS fitting parameters: 0.700 < S_0^2 < 1.000; CN > 0; σ^2 > 0 Å^2; ΔE_0 < 10 eV; R factor < 0.02

Table S2. Fe-EXAFS data fitting results of FeCu-NCNT.

Sample	Scattering pair	CN	R (Å)	σ^2(Å^2)	ΔE_o (eV)	R-factor
FeCu-PCNF	Fe-N1	1.9	1.922+0.023	0.0033	12.98	0.007
	Fe-N2	2.2	1.945+0.10	0.0018		
	Fe-Cu	0.8	2.412+0.04	0.0011		
Fe-NCNT	Fe-N	4.04	1.928+0.03	0.0014	5.96	0.0014

CN represents coordination number, R represents interatomic distance, σ^2 indicates the Debye-Waller factor value, ΔE_o represents edge-energy shift, and R-factor represents goodness of the fit. Error bounds (accuracies) that characterize the structural parameters obtained by EXAFS spectroscopy were estimated as CN ± 20%; R ± 1%; σ^2 ± 20%; ΔE_0 ± 20%. S_0^2 was fixed to 1.1, which is according to the experimental EXAFS fit of Co foil by fixing CN as the known crystallographic value. Fitting range:2.0 ≤ k (/Å) ≤ 13 and 1 ≤ R (Å) ≤ 5; A reasonable range of EXAFS fitting parameters: 0.700 < S_0^2 < 1.000; CN > 0; σ^2 > 0 Å^2; ΔE_0 < 10 eV; R factor < 0.02.

Table S3. Comparison of ORR performance of FeCu-NCNT at 1600 rpm in 0.1 M KOH with FeCu-NCNT electrocatalysts in recent reported literatures.

Catalysts	**$E_{1/2}$ (V)**	**E_0 (V)**	**References**
FeCu-NCNT	0.88	~0.98	**This work**
o-MQFe-10:20:5	0.861	~0.98	*Angew. Chem., Int. Ed. 2022, 61, 202117617*
FePc/CoPc HS	0.879	0.971	*Adv. Funct. Mater. 2020, 30, 2005000*
Fe-ND/C	0.79	0.91	*Nano Res. 2021, 14, 1069-1077*
Fe SA-NSC-900	0.86	0.94	*ACS Energy Lett. 2021, 6, 379-386*
$Ti_4N_3O_x$/FePc	0.87	~0.98	*Adv. Energy Mater. 2024, 2403899*
FeSA/FeAC@PPy/CC	0.83	0.93	*Energy Environ. Sci., 2025, 18, 2839–2851*
Zn-N-C-1	0.873	0.96	*Angew. Chem. Int. Ed., 2019, 58, 7035-7039*
Fe/CuSAs-Mag	0.86	1.57	*Angew. Chem. Int. Ed. 2023, 62 e2022304229*
H-3DOM-Co/ONC	0.876	0.94	*Adv. Mater. 2023, 35, 2301894*
Fe–N@Ni–HCFs	0.88	0.935	*Adv. Funct. Mater., 2022, 32, 2209273*
FePc NTs-rGO	0.88	0.97	*Proc. Natl. Acad. Sci. USA **2024**, 121, e2316553121*
FePc-DNA-rGO	0.855	0.93	*ACS Catal. **2024**, 14, 7514*
FePc@CNF	0.875	0.966	*Chem. Eng. J. **2024**, 483, 149243*
FePc/CoPc HS	0.879	0.971	*Adv. Funct. Mater.* **2020**, 30, 2005000

Table S4. The comparison of Zn-air batteries performance between FeCu-NCNT and previously reported electrocatalysts.

Electrocatalysts	Catalyst loading (mg cm^2)	Power density (mW cm^2)	Specific capacity (mAh g^{-1})	References
FeCu-NCNT	**1**	**186.9**	**788**	**This work**
Fe_{ACs}/NPS	1	172.4	863.5	*Angew. Chem.Int. Ed.2023,62, e2023141*
FeN_3O-O-Ti	1	158	807.8	*Angew. Chem. Int. Ed. 2022, 61, 61, e2021*
CR-Co/ClNC	1	176.6	745	*Nature Communications | (2024) 15:1675*
Fe SACs HS	1	170	-	*Angew. Chem. Int. Ed. 2023, 62, e202304229*
Au SAC CoN@NF	1	161.94	813.80	*Adv. Funct. Mater.2024, 2316699*
$Fe_{SA/AC}$@HNC	1	171.5	811.8	*Adv. Mater. 2024, 2400523*
CoSA/N, S-HCS	1	173.1	781.1	*Adv. Energy Mater., 2020, 2002896*
N-FeN_4	1	171	772	*Adv. Funct. Mater. 2024, 2409794*
CoFeN-NCNTs/CCM	1	145	778	*Adv. Funct. Mater., 2021, 2107608*
Co_2P/CoN_4@NSC-500	1	134.5	-	*Angew.Chem.Int. Ed.2023*,62, e202216950

References

[1] G. Kresse, J. Furthmüller, *Comput. Mater. Sci.* 1996, **6**, 15.

[2] P. E. Blochl, *Phys. Rev. B* 1994, **50**, 17953.

[3] G. Kresse, J. Furthmüller, *Phys. Rev. B* 1996, **54**, 11169.

[4] J. P. Perdew, K. Burke, M. Ernzerhof, *Phys. Rev. Lett.* 1996, **77**, 3865.

[5] S. Grimme, J. Antony, S. Ehrlich, H. Krieg, *J. Chem. Phys.* 2010, **132**, 154104.

[6] A. L. Han, X. J. Wang, K. Tang, Z. D. Zhang, C. L. Ye, H. B. Hu, L. R. Zheng, P. Jiang, C. X. Zhao, Q. Zhang, D. S. Wang, Y. D. Li, *Angew. Chem. Int. Ed.* 2021, 60, 19262–19271.